Ultrafine Grain Refinement of Biomedical Co-29Cr-6Mo Alloy during Conventional Hot-Compression Deformation

KENTA YAMANAKA, MANAMI MORI, SHINGO KUROSU, HIROAKI MATSUMOTO, and AKIHIKO CHIBA

In order to examine the microstructural evolution during hot-compression deformation of the biomedical Co-29Cr-6Mo (weight percent) alloy without the addition of Ni, hot-compression tests have been conducted at deformation temperatures ranging from 1050 °C to 1200 °C at various strain rates of 10^{-3} to 10 s^{-1}. The grain refinement due to dynamic recrystallization (DRX) was identified under all deformation conditions by means of field-emission scanning electron microscopy/electron backscattered diffraction (FESEM/EBSD) and transmission electron microscopy (TEM) observations. Although the DRX grain size (d) of the deformed specimens considerably decreased with an increasing Zener–Hollomon (Z) parameter at strain rates ranging from 10^{-3} to 0.1 s^{-1}, a grain size coarser than that predicted from the d-Z relation was obtained at strain rates of 1.0 and 10 s^{-1}. An ultrafine-grained microstructure with a grain size of approximately 0.6 μm was obtained under deformation at 1050 °C at 0.1 s^{-1}, from an initial grain size of 40 μm. The grain refinement to a submicron scale of biomedical Co-Cr-Mo alloys has been achieved with hot deformation by ~60 pct due to DRX, in which the bulging mechanism is not operative. The ultrafine grains obtained due to DRX without bulging is closely related to the considerably low stacking-fault energy (SFE) of the Co-Cr-Mo alloy at deformation temperatures.

DOI: 10.1007/s11661-009-9879-0

I. INTRODUCTION

ALLOYS of Co-Cr-Mo have been extensively used in biomedical implants such as artificial hip and knee joints because of their excellent corrosion and wear resistance as well as their good mechanical properties. Although Co-Cr-Mo alloys are frequently used in the as-cast condition, they exhibit a coarse dendritic microstructure with many flaws, such as interdendritic microvoids, precipitations, and segregation of solute atoms, which are formed during solidification. Therefore, the strength of these alloys in the as-cast condition is extremely low. It is thus important to enhance their strength for practical applications by eliminating inherent defects through the application of thermomechanical treatments.[1]

Grain refinement is being investigated for various metals and alloys, because it enhances strength without sacrificing toughness. In particular, ultrafine grains smaller than 1 μm and nanocrystalline ($d < 100$ nm) alloys have been produced not by microstructure control achieved using conventional thermomechanical processing but by severe plastic deformation (SPD).[2–8] Various SPD techniques have been proposed, including equal-channel angular pressing (ECAP),[2–4] high-pressure torsion,[2] accumulative roll-bonding,[5,6] and multidirectional forging.[7,8] Although grain refinement is an effective strengthening method that is independent of alloy design, there have been no reports of the application of SPD techniques to Co-Cr-Mo alloys. This is because Co-Cr-Mo alloy forms a dual-phase microstructure due to a martensitic transformation during cooling to room temperature and straining. This dual phase consists of a metastable fcc γ phase and an hcp ε phase and it suffers from poor ductility. In addition, the application of SPD is also limited by the high work hardening generated by the strain-induced martensitic transformation during plastic deformation caused by the instability of the γ phase. Moreover, according to the Co-Cr-Mo ternary phase diagram,[4] when Co-Cr-Mo alloy is held at high temperatures, there is a high probability that it will precipitate the σ phase (CoCr: $P42/mnm$). This can act as a starting point of fracture, making it difficult to simultaneously suppress the σ phase, using microstructure control in conjunction with static recrystallization (SRX), and perform grain refinement. Therefore, when plastically forming the alloy, a large amount of Ni (10 to 37 mass pct) is generally added to Co-Cr-Mo alloys to improve their ductility by stabilizing the γ phase (the high-temperature phase) at room temperature. However, using Ni in biomaterials is problematic, because it can cause allergies or cancer in

KENTA YAMANAKA, Graduate Student, formerly with the Department of Materials Processing, Graduate School of Engineering, Tohoku University, is with Kobe Steel, Ltd., Kobe 651-8585, Japan. MANAMI MORI, Graduate Student, formerly with the Department of Materials Processing, Graduate School of Engineering, Tohoku University, is with Nissan Arc, Ltd., Yokosuka 237-0061, Japan. SHINGO KUROSU, Postdoctoral Student, HIROAKI MATSUMOTO, Assistant Professor, and AKIHIKO CHIBA, Professor, are with the Institute for Materials Research, Tohoku University, Sendai 980-8577, Japan. Contact e-mail: a.chiba@imr.tohoku.ac.jp
Manuscript submitted January 30, 2009.
Article published online June 20, 2009

living organisms. Hence, it is important to establish microstructure control methods that do not involve cold deformation and subsequent annealing (*i.e.*, SRX). One candidate is hot-deformation processing that improves mechanical properties and simultaneously eliminates the σ phase in Ni-free Co-Cr-Mo alloys.

Numerous studies have been conducted on the dynamic recrystallization (DRX) that occurs during the hot working of metals and alloys with relatively low stacking-fault energies (SFEs), such as Cu, Ni, and austenitic stainless steels.[9–12] For example, it has been reported that fine grains (approximately 2 μm) can be developed by the hot deformation of austenitic stainless steel, which is an alloy with one of the lowest SFEs at room temperature.[10] These studies pointed out that the operation of the discontinuous DRX accompanied by the nucleation and growth of new grains is considered to be the principal source of grain refinement. The nucleation of DRX has been explained in terms of a bulging mechanism[11] that occurs as a result of the strain-induced grain boundary (GB) migration that is due to inhomogeneous local strain gradients induced during high-temperature deformation. In this mechanism, serrated GBs have been observed prior to nucleation and these have been verified in Cu and Ni by means of crystal orientation analysis and other techniques.[11,12] Dynamic recrystallization has also been observed in interstitial-free and ferritic stainless steels, both of which had been previously assumed to have dynamic recovery mechanisms (*i.e.*, DRX is not operative) because of their high SFEs.[13,14] Generally, DRX produces finer grains than SRX, because grain growth after recrystallization is almost negligible in DRX. While both mechanisms produce grains with a minimum size of several micrometers, the use of DRX is extremely important in refining grains in hot-deformation processing. The Co-Cr-Mo alloys are considered to have low SFEs, because they readily undergo martensitic transformations during cooling and plastic deformation. Thus, by suitable selection of hot-working conditions, it is anticipated that considerable grain refinement can be obtained by using DRX.

In order to definitively demonstrate the occurrence of DRX, it is necessary to confirm the following two points (as noted by Tsuji *et al.*): (1) that new grains are surrounded by high-angle GBs (HAGBs) and (2) that new grains are generated during high-temperature deformation.[13,14] However, although grain refinement by hot forging has been reported in Co-28Cr-6Mo (weight percent) alloy,[1] which is the representative composition of the ASTM F75 standard, the occurrence of DRX has not been investigated. Studies have so far been primarily conducted on hot or warm working in single-phase regions, and very little has been reported on alloy systems such as Co-Cr-Mo alloys, which exhibit a complex phase stability that allows them to readily transform martensitically. Moreover, DRX behavior is substantially affected by the SFE, the value of which depends on both the composition and the temperature. It is thus necessary to pay attention to both the process temperature and the chemical composition when investigating DRX behavior and to ascertain whether there is any addition of γ-phase stabilizing elements (*e.g.*, Ni, N, and C) in the case of Co-Cr-Mo alloys.

The aim of the present study is to conduct hot-compression tests on Co-Cr-Mo alloys that do not contain additional γ-phase stabilizers, such as Ni, N, and C, for a variety of conditions (*i.e.*, deformation temperature, strain rate, and strain), to obtain basic knowledge on high-temperature deformation behavior and grain refinement by DRX. A further aim of this study is to employ a thermodynamic model to estimate the SFE at deformation temperatures, in order to assess the effect of SFE on DRX behavior.

II. EXPERIMENTAL PROCEDURE

An ingot (with a top diameter of 80 mm, bottom diameter of 70 mm, and height of 120 mm) with a mass of approximately 5 kg and a nominal composition of Co-29Cr-6Mo (weight percent) was prepared by high-frequency vacuum-induction melting. The obtained ingot was subjected to homogenizing heat treatment at 1225 °C for 12 hours, followed by hot forging and hot swaging at 1200 °C. It was finally formed as a 14-mm-diameter rod, which was water quenched to room temperature. Table I shows the composition of this rod. Cylindrical specimens (8 mm in diameter and 12 mm in height) were cut from the rod using an electrical discharge machine; they were subjected to a hot-compression test under vacuum using a hot-deformation simulator (Thermec Master-Z, Fuji Electronic Industrial Co., Ltd., Saitama, Japan). A uniaxial compression test was conducted with a maximum compressive strain of 60 pct (true strain: $\varepsilon = 0.92$) while varying the deformation temperature within the γ-phase stable region of 1050 °C to ~1200 °C and a strain rate within the range of 10^{-3} to ~10 s^{-1}; the number of sampling data points in the compression tests is 1024, regardless of strain rates. The specimen was heated to 1200 °C at a rate of 5 °C s^{-1} by high-frequency induction heating; it was subjected to homogenizing heat treatment for 300 seconds after reaching the target temperature. After the test, it was cooled to room temperature using a N_2-He gas mixture at a cooling rate of 50 °C s^{-1}. In order to study the microstructural changes induced by hot deformation, another specimen without any deformation (hereafter, termed "the undeformed specimen") was produced by holding the specimen at 1200 °C for 300 seconds, cooling it to its deformation temperature, and further gas cooling it to room temperature without any deformation.

In the hot-compression test, barreling occurs due to friction at the contact surfaces between the cylindrical specimen and the anvil. In addition, there is a possibility

Table I. Chemical Composition of Material Used in This Study (Weight Percent)

Co	Cr	Mo	Ni	C	Si	O	N
Balance	29.25	5.84	0.05	0.020	0.01	0.0056	0.001

of work heating due to adiabatic deformation as a result of conducting the compression test with a relatively high strain rate. Therefore, the effects of friction and work heating during hot deformation on the stress-strain relation were compensated, in accordance with the procedures given in References 15 and 16.

Microstructural observations were conducted by field-emission scanning electron microscopy (FESEM) (XL30S-FEG, PHILIPS*) and transmission electron microscopy (TEM) (2000EX, JEOL**). The SEM observations were performed at approximately the center of a longitudinal section that passes through the center of the bottom surfaces of the hot-compression specimen and that is parallel to the compression axis. The constituent phases were identified by X-ray diffraction (XRD) (X'Pert MPD, PHILIPS). Moreover, crystallographic analysis was conducted by electron backscatter diffraction (EBSD) using an orientation-imaging microscope (TexSEM Laboratories, Inc., Provo, UT) attached to the field-emission scanning electron microscope. The acceleration voltage during the FESEM measurements was 30 kV (beam current: approximately 100 μA). The surface of the specimen for the microstructural observation was prepared by first dry grinding using SiC emery paper (grades 180 to 3000), and then mirror finishing using a suspension of 0.3-μm Al_2O_3 and 0.04-μm colloidal silica. Electrolytic polishing was subsequently conducted in a sulfuric acid-methanol (1:9) solution, in order to observe the GBs and remove the surface-worked layer produced by grinding. A Vickers hardness test was performed on the cross section of the specimen, in order to study the mechanical characteristics resulting from grain refinement. The TEM specimen was produced by cutting a 3-mm-diameter disk from the center of the compression test specimen parallel to the compression axis and grinding it to form a thin film using a dimple grinder. Finally, the thin foils for TEM observations were prepared by ion-beam milling (M691, Gatan†) at 3 keV.

Several methods have been proposed for estimating the SFE. In addition to estimating the SFE directly from the stacking-fault width determined by TEM, it can be determined by both an XRD-based method[17] and a method based on thermodynamic calculations.[18,19] In the present study, the SFE in the temperature range in which the hot-compression test was conducted was estimated from a thermodynamic model proposed by Olson and Cohen.[20] The thermodynamic parameters required for the SFE calculation were calculated using Thermo-Calc software (Thermo-Calc Software, Stockholm), which is a well-known package for thermodynamic calculations.

*PHILIPS is a trademark of Philips Electronic Instruments Corp., Mahwah, NJ.

**JEOL is a trademark of Japan Electron Optics Ltd., Tokyo.

†Gatan is a trademark of Gatan, Inc., Warrendale, PA

III. RESULTS

A. *Hot-Deformation Behavior*

Figures 1(a) and (b) show the effect of deformation temperature and strain rate on the true stress-true strain (σ-ε) curves obtained from the hot-compression tests. Figure 1(a) shows the σ-ε curves obtained at various temperatures from 1050 °C to 1200 °C at a fixed strain rate of 10 s^{-1}; Figure 1(b) shows the results when the strain rate was varied at a fixed temperature of 1150 °C. These σ-ε curves are those obtained after compensating for friction and work heating. For all the deformation conditions, the σ-ε curves exhibit typical DRX characteristics; specifically, the flow stress increases to a peak stress followed by work softening and steady-state flow is attained at higher strains. Furthermore, all the obtained σ-ε curves have a single peak; neither the

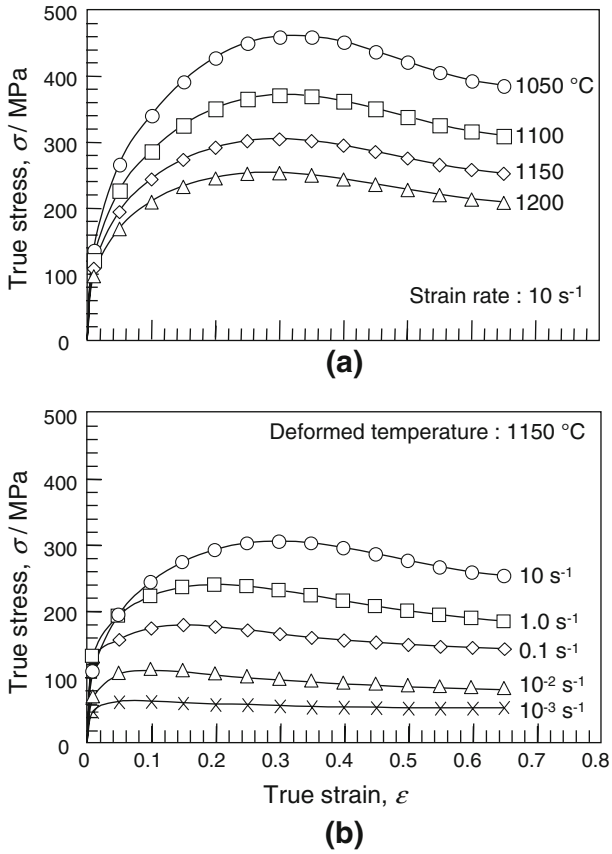

Fig. 1—True-stress–true-strain curves after the compensation for friction and adiabatic heating of Co-29Cr-6Mo alloy in hot-compression tests (*a*) at a fixed strain rate of 10 s^{-1} at various temperatures and (*b*) at a fixed deformation temperature of 1150 °C at various strain rates.

stress oscillations in the σ-ε curves having multiple stress peaks nor dynamic recovery in σ-ε curves for the case in which steady-state flow develops without work softening were observed. Figure 2 shows the relationship between the peak stress σ_p and the strain corresponding to the peak stress (hereafter referred to as the peak strain ε_p) for each compression condition. As shown in Figure 2, ε_p increases with an increasing σ_p. On the other hand, a different linear relationship between ε_p and σ_p is observed at a strain rate of 10 s^{-1}; in addition, the peak stress exhibits a trend associated with athermal deformation, namely, it has a smaller dependence on temperature. Warm- and hot-compression test results for SUS304 stainless steel[10] reveal that the transition to athermal deformation is due to the deformation mechanism changing from hot to warm deformation. It is thus possible that a similar change in the deformation mechanism may be reflected in the present results for Co-Cr-Mo alloys.

Figure 3 shows the strain-rate dependence of the 0.2 pct yield stress obtained from the σ-ε curve for the hot-compression test. Although the 0.2 pct yield stress increases with an increase in the strain rate, it decreases toward 10 s^{-1} from the peak at 0.1 or 1.0 s^{-1}. In other words, the strain-rate sensitivity m becomes negative for strain rates in the range from 0.1 to 10 s^{-1}. According to Prasad, the factors that can cause m to become negative are dynamic strain aging (DSA), deformation twins, shear bands, and the formation/propagation of microcracks.[20] A similar phenomenon has also been confirmed in hot-compression tests of Co-28Cr-6Mo-0.16N (weight percent) alloy, the γ phase of which is more stable than the present Co-29Cr-6Mo alloy, due to the addition of nitrogen. Based on these tests, it was concluded that DSA and the formation of deformation twins cause m to become negative.[21–23] Because deformation twins and shear bands have rarely been identified in the hot-compressed specimens of Co-29Cr-6Mo

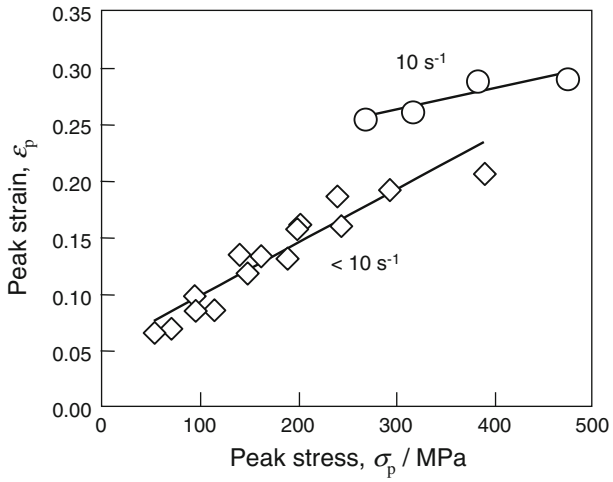

Fig. 2—Relationship between peak strain and peak stress for Co-29Cr-6Mo alloy in hot-compression tests.

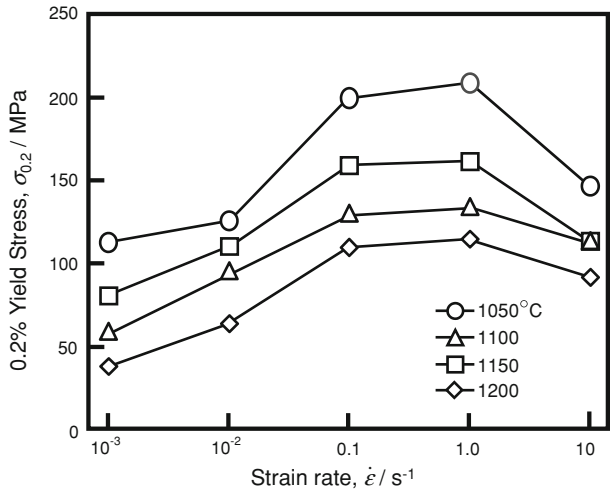

Fig. 3—Variation of 0.2 pct yield stress of Co-29Cr-6Mo alloy as a function of strain rate in hot-compression tests at elevated temperatures.

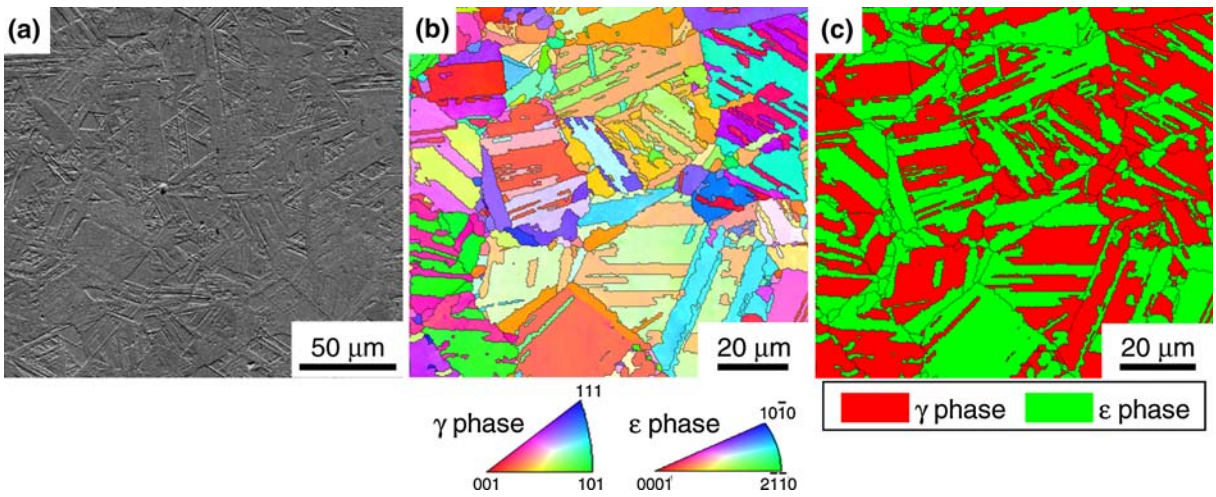

Fig. 4—Initial microstructure of Co-29Cr-6Mo alloy heat treated at 1150 °C for 300 s: (*a*) SEM image, (*b*) IPF map, and (*c*) phase map.

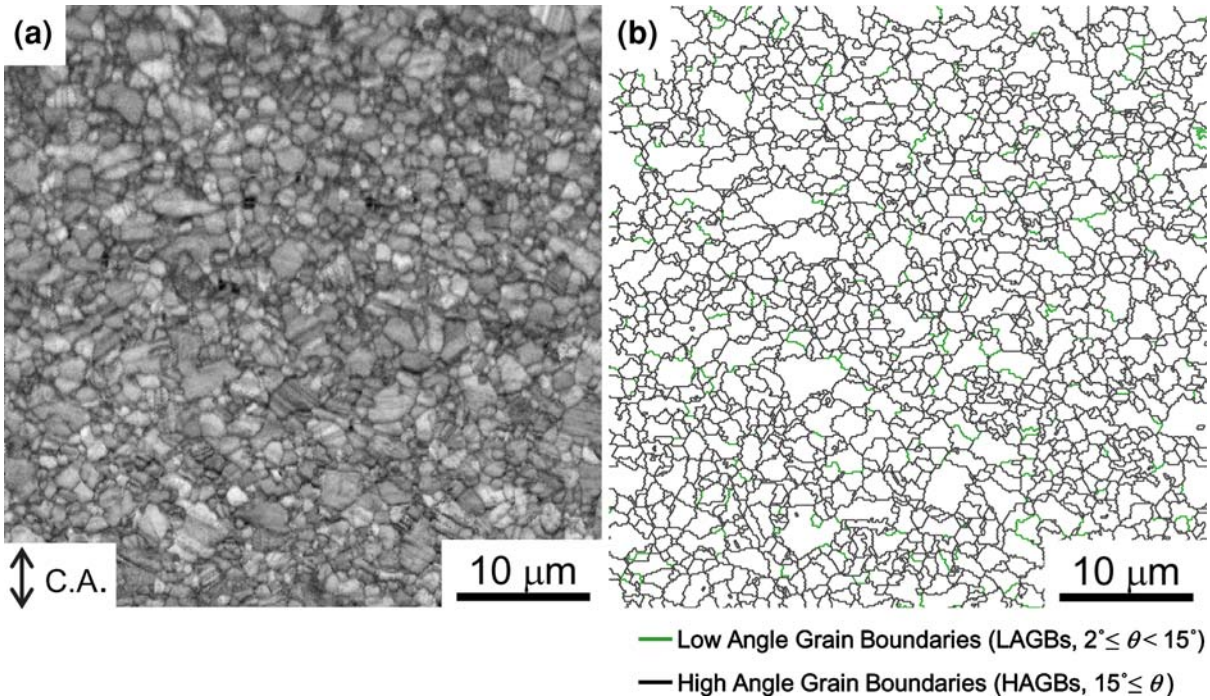

Fig. 5—Microstructure of Co-29Cr-6Mo alloy compressed to 60 pct at 1150 °C at 1.0 s^{-1}: (*a*) IQ map and (*b*) GB map. Black and green lines represent the HAGBs and LAGBs, respectively.

alloy (Section B), DSA is considered to be the origin of the negative strain-rate sensitivities. However, the details need to be clarified in future studies.

B. *Microstructural Evolution Due to Hot Deformation*

Figures 4(a) through (c) show a SEM micrograph and EBSD maps of the initial microstructure prior to deformation, which is subjected to homogenizing heat treatment at 1200 °C, held at 1150 °C, and then quenched to room temperature. They show that the microstructure consists of equiaxed grains, and no precipitation of the σ phase is observable in the SEM micrograph (Figure 4(a)). Some grains having striations are visible. From the inverse pole figure (IPF) map shown in Figure 4(b) and the phase map shown in Figure 4(c), these striations are judged to be in the ε phase, which was formed by a martensitic transformation during cooling. The grain size at the deformation temperature that is equivalent to the size of the initial γ grains at room temperature is approximately 40 μm.

Figures 5(a) and (b) show the microstructure of the specimen compressed by 60 pct ($\varepsilon = 0.92$) at 1150 °C at a strain rate of 1.0 s^{-1}. These figures represent typical changes in the microstructure produced by hot deformation. Figure 5(a) is an image quality (IQ) map and Figure 5(b) is a GB map obtained by the EBSD measurement. The IQ map of Figure 5(a) shows that the specimen after hot compression has an equiaxed grain structure and the mean grain size is reduced to approximately 1.6 μm. In addition, the GB map reveals that the grains are largely surrounded by HAGBs that have a misorientation greater than 15 deg. This was true for all the specimens subjected to the hot-compression test for all the different test conditions. In other words, new fine grains were formed during hot deformation with a relatively low true strain of less than 1. Figure 6 shows XRD profiles of specimens subjected to hot compression at 1150 ° C at various strain rates. The formation of the ε phase is extremely suppressed at strain rates in the range 0.1 to 1.0 s^{-1} compared to lower strain rates. The suppression of athermal martensitic transformations[24] is conjectured to be a result of grain refinement to smaller than 10 μm. Moreover, no peaks indicating the precipitation of the σ phase were observed.

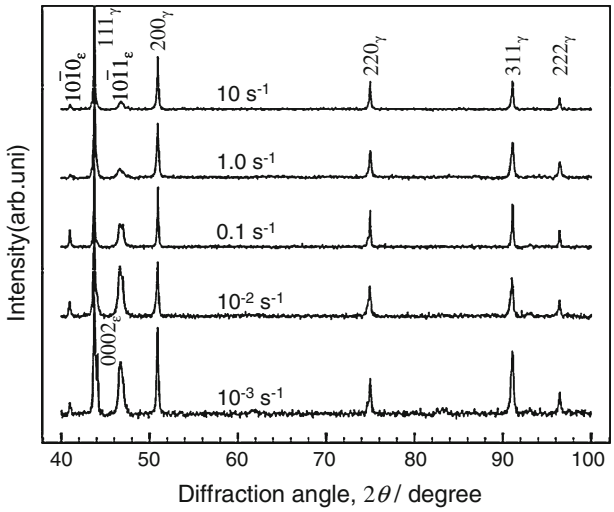

Fig. 6—XRD profiles of specimens after hot-compression tests at 1150 °C.

Figures 7(a) through (c) show the TEM microstructure for the specimen compressed by 60 pct at a

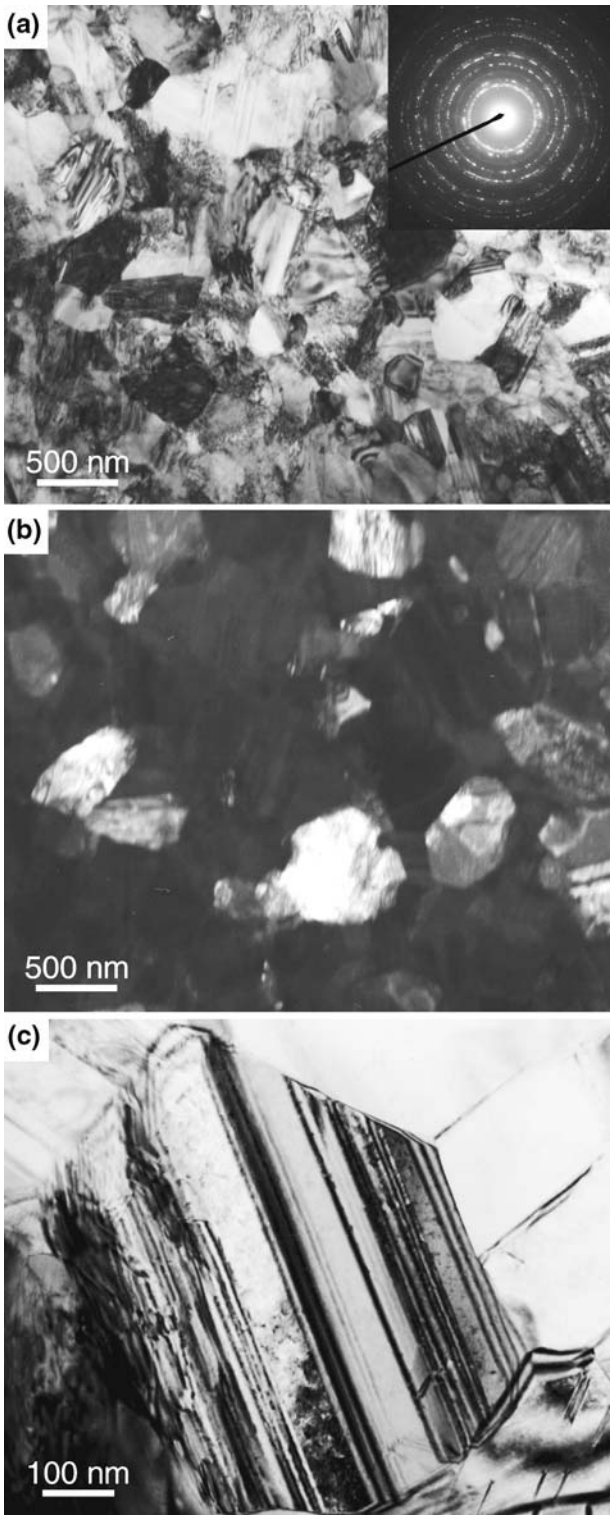

Fig. 7—TEM microstructure of recrystallized grain in cross section of a specimen after compression by 60 pct at 1050 °C at 0.1 s^{-1}: (*a*) bright-field image, (*b*) dark-field image, and (c) magnified bright-field image of the recrystallized grain.

deformation temperature of 1050 °C and a strain rate of 0.1 s^{-1}. The mean grain size that generated the finest structure in this study is extremely small, less than 1 μm, and the individual crystal orientations were relatively

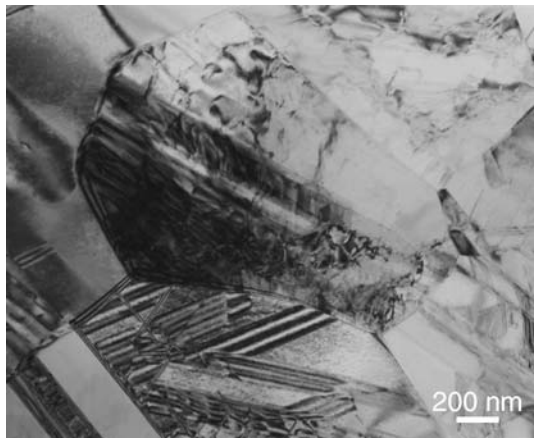

Fig. 8—TEM bright-field image of recrystallized grains in the cross section of a specimen after compression by 60 pct at 1050 °C at 10 s^{-1}.

random, based on the fact that the selected-area diffraction (SAD) pattern shown in Figure 7(a) is ring shaped. In addition, the grains have a dark contrast, suggesting a high density of dislocations. This is in contrast with statically recrystallized grains, which generally have extremely low dislocation densities. The grains also exhibit numerous stacking faults (Figure 7(c), which is a magnified image of Figure 7(a)). The typical TEM microstructure after compression by 60 pct at a strain rate of 10 s^{-1} at 1050 °C is shown in Figure 8. These are microstructures characteristic of the present alloy after hot deformation. Because the specimen was rapidly cooled after compression, these lattice defects are assumed to be formed during the hot-deformation process. Therefore, it is concluded that the grains were refined by DRX. This is based on the fact that these grains differ from statically recrystallized grains that have an extremely low dislocation density; specifically, they are surrounded by HAGBs.

C. *Effect of Deformation Conditions on DRX Behavior*

Figures 9(a) through (e) show IQ maps of the specimens hot compressed by 60 pct at 1150 °C at various strain rates. The strain rate exerts a large effect on grain refinement when it is in the range 10^{-3} to 1.0 s^{-1}, and the grain size becomes extremely refined as the strain rate increases. On the other hand, the grains produced at a strain rate of 10 s^{-1} are coarser than those produced at 1.0 s^{-1}. In other words, grain refinement due to DRX increases markedly with an increasing strain rate, up to 1.0 s^{-1}, at which point the refining behavior changes, up to a strain rate of 10 s^{-1}. This tendency was not limited to a deformation temperature of 1150 °C; it was also observed at the other deformation temperatures. Figure 10 shows the results of a Vickers hardness test, specifically, that the Vickers hardness decreases when the strain rate reaches 10 s^{-1}, in a manner similar to the dependence of grain refinement on the strain rate; the increase in the grain size shown in the IQ map is considered to be the principal reason for this.

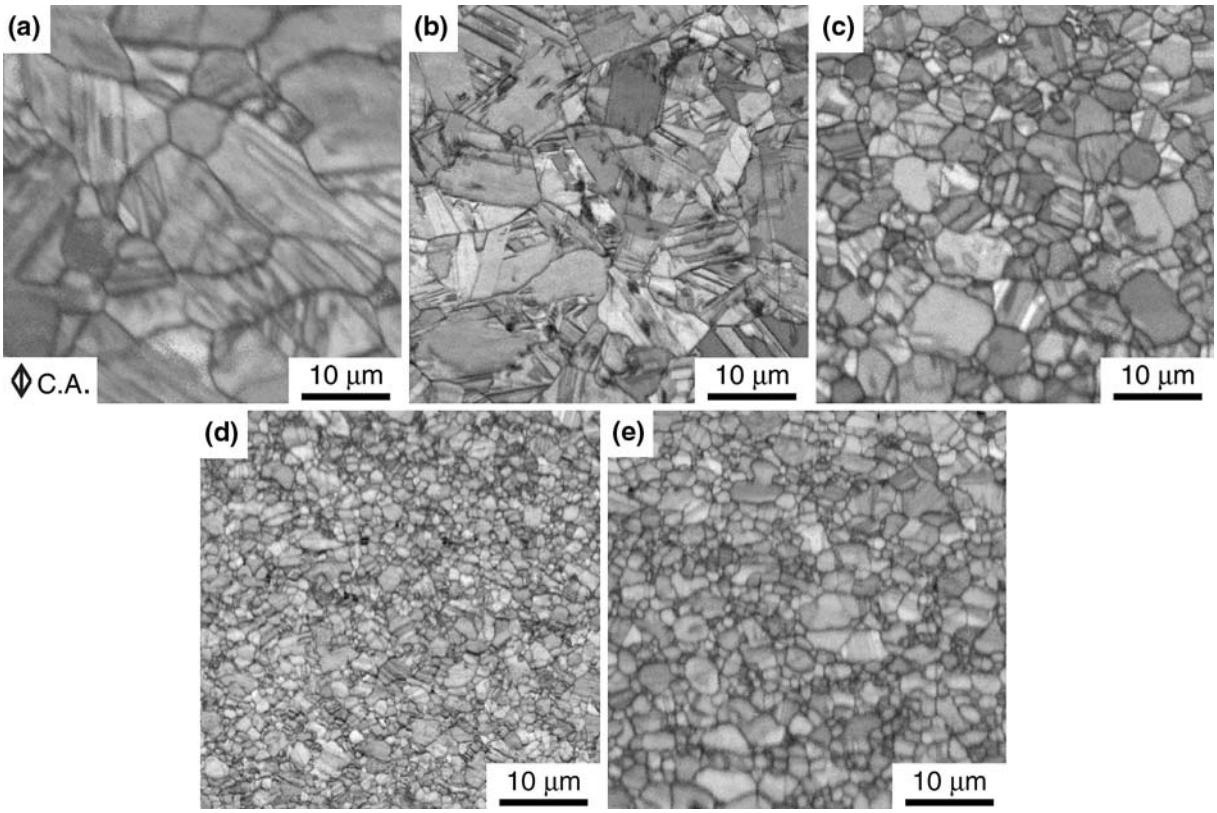

Fig. 9—Effect of strain rate on microstructure evolution of Co-29Cr-6Mo alloy deformed to true strain of 0.92 at 1150 °C at (*a*) 10^{-3}, (*b*) 10^{-2}, (*c*) 0.1, (*d*) 1.0, and (*e*) 10 s^{-1}.

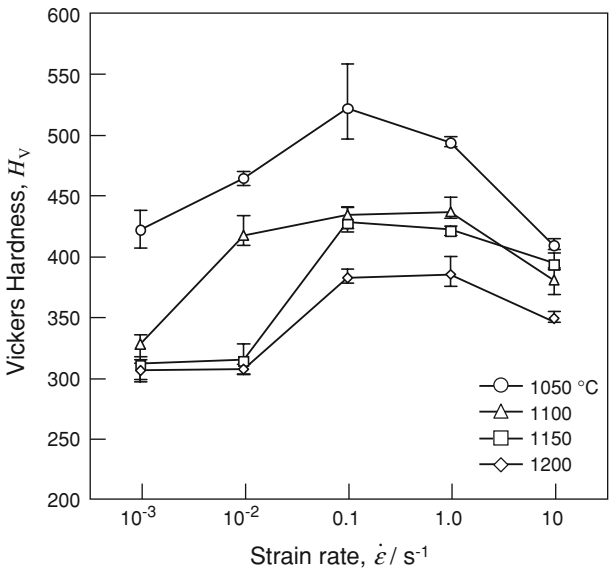

Fig. 10—Variation of Vickers hardness of as-hot-compressed specimens with strain rate.

Figures 11(a) through (d) show the effect of strain on grain refinement. In the microstructure observation results (Figure 11(a)) at a compression of 5 pct, which roughly corresponds to the yield point in the σ-ε curve for a deformation temperature of 1150 °C at a strain rate of 10 s^{-1}, they reveal a deformed microstructure the grain sizes of which are just as coarse as those of the undeformed material. The grains are elongated in the direction perpendicular to the compression axis. No refining of the grains is observable. At 10 pct compression (Figure 11(b)), equiaxed grains are observed that are finer than the initial grains but coarser than grains produced at a compression of 60 pct. The grains gradually become finer as deformation advances, but they are not completely refined at a compression of 30 pct (Figure 11(c)). Moreover, nucleation of DRX at a low strain generally advances *via* bulging, which is confirmed to occur even after the peak stress is reached in the high-temperature deformation of Fe-Ni-C alloys.[25] However, no recrystallization nucleation due to serration of the initial γ GBs and bulging is observed, even at low strain rates, in the case of the Co-29Cr-6Mo alloy.

IV. DISCUSSION

A. *Relationship between Deformation Conditions and DRX Behavior*

Dynamic recrystallization behavior is greatly affected by the deformation conditions (*i.e.*, the deformation temperature and strain rate). In this section, the relationship between the hot-compression conditions and the DRX behavior was expressed in terms of the Zener–Hollomon (Z) parameter.

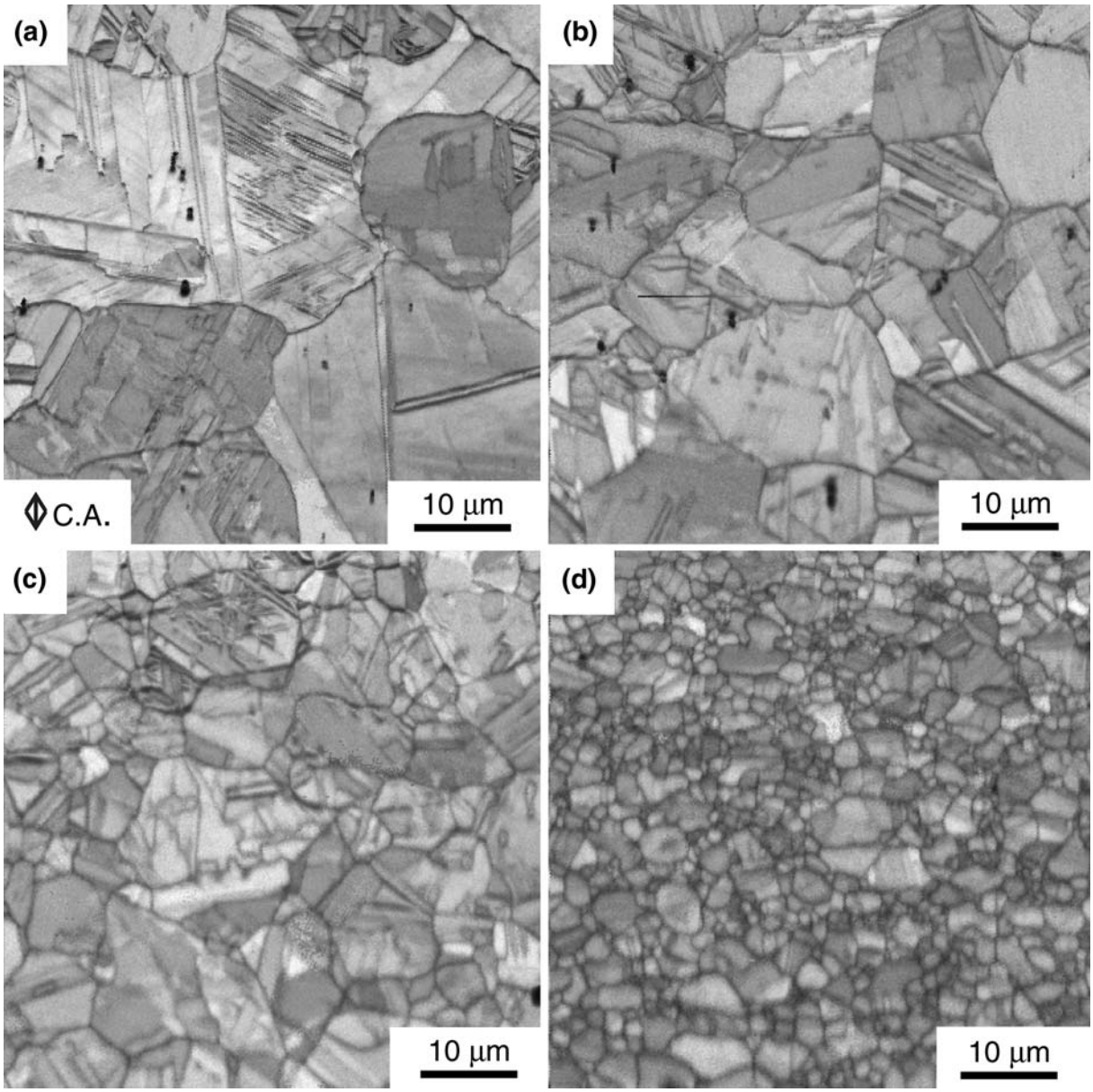

Fig. 11—Microstructure evolution deformed at 1150 °C at 10 s^{-1} at a strain of (*a*) 5, (*b*) 10, (*c*) 30, and (*d*) 60 pct.

In general, the DRX behavior at high temperatures can be expressed in terms of the strain rate, including the Arrhenius-type temperature-dependent term. The Z parameter was calculated using the following equation, which is valid over the entire stress range used in this study:[26]

$$Z = \dot{\varepsilon} \exp\left(\frac{Q}{RT}\right) = A\left[\sinh\left(\alpha\sigma_p\right)\right]^n \qquad [1]$$

where $\dot{\varepsilon}$ is the strain rate, Q is the apparent activation energy of high-temperature deformation, R is the gas constant, T is the deformation temperature, σ_p is the peak stress, n is the stress exponent, and A is a constant. The activation energy Q is the mean value obtained using the following equation:

$$\begin{aligned} Q &= R \cdot \left.\frac{\partial \ln \dot{\varepsilon}}{\partial \ln\left[\sinh\left(\alpha\sigma_p\right)\right]}\right|_T \cdot \left.\frac{\partial \ln\left[\sinh\left(\alpha\sigma_p\right)\right]}{\partial(1/T)}\right|_{\dot{\varepsilon}} \\ &= R \cdot n \cdot \left.\frac{\partial \ln\left[\sinh\left(\alpha\sigma_p\right)\right]}{\partial(1/T)}\right|_{\dot{\varepsilon}} \end{aligned} \qquad [2]$$

where α is the fitting parameter. A good linear relationship is obtained when $\alpha = 0.0056$, as shown in Figures 12(a) and (b). Table II gives the material constants used in the calculation for the Co-29Cr-6Mo alloy. The activation energy for high-temperature deformation is 561.85 kJ mol^{-1}, which is greater than that for the self-diffusion of pure cobalt (440 kJ mol^{-1}).[27] Similar tendencies have also been reported for other alloys, including Ti alloys and Ni-based superalloys.[15,28,29]

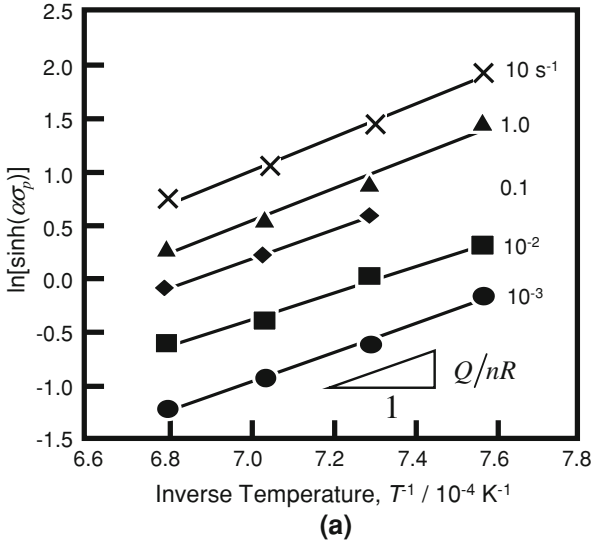

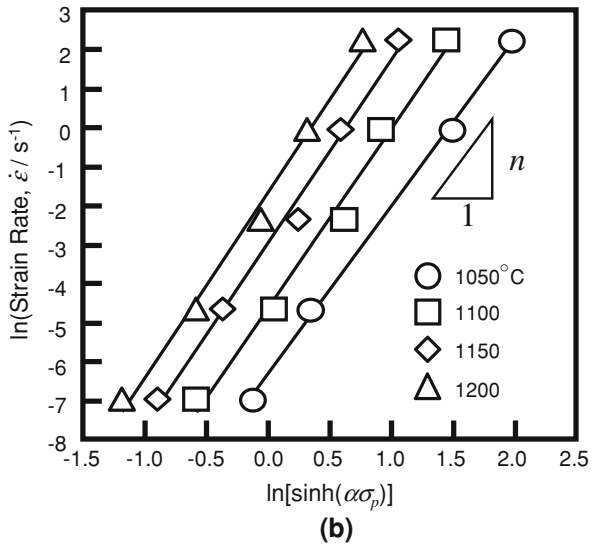

Fig. 12—Correlation of the peak flow stress to (*a*) deformation temperature and (*b*) strain rate based on Eq. [2].

Table II. Material Constant in Co-29Cr-6Mo Alloy

A (s^{-1})	n	α (MPa^{-1})	Q (kJ mol^{-1})
1.64×10^{19}	4.68	0.0056	561.85

This is thought to be because DRX is more a dominant deformation mechanism than dynamic recovery, which is diffusion limited.[28] On the other hand, precipitation effects have been observed in Ni-based superalloys[15] and Mg-Al-Zn alloys.[29] In the case of the present alloy, as is clear from the discussion of the TEM observation results and the SFE (described later), dislocations are dissociated into Shockley partials bounding the stacking fault, so that they are unlikely to cause cross slip or dislocation climb. Therefore, it is thought that the high-temperature deformation mechanism does not depend only on the dislocation recovery but is related to the interactions of the dislocations and solute elements in a complex way that contributes to the increase in the apparent activation energy.

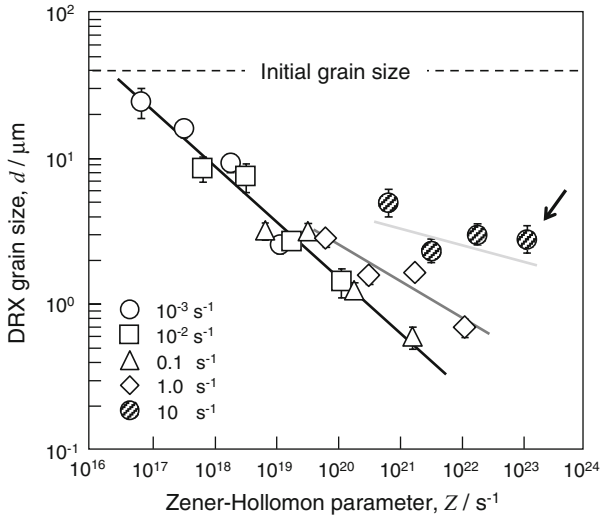

Fig. 13—Relationship between Z parameter and grain sizes in the hot-deformed specimens.

In Figure 13, the grain size d after DRX is plotted against the Z parameter. The grain size is calculated using the IQ map obtained from the EBSD measurements. The grain size after DRX generally decreases with an increase in the Z parameter. Figure 13 shows that the correlation expressed by the following equation holds for strain rates in the range of 10^{-3} to ~0.1 s^{-1} for the Co-29Cr-6Mo alloy:

$$d = 5.6 \times 10^{7} \cdot Z^{-0.38} \qquad [3]$$

The minimum grain size of the Co-29Cr-6Mo alloy obtained by DRX is approximately 0.6 μm, which is far smaller than the size of dynamically recrystallized grains obtained after compression testing of SUS304 austenitic stainless steel, which is a low-SFE alloy.[10,30] At high strain rates of 1.0 and 10 s^{-1}, the d-Z relation changes in such a way that a microstructure is observed that has grains coarser than the crystal grain sizes predicted by Eq. [3]. This demonstrates that the d-Z relations differ from those predicted by Eq. [3] and that the Z parameter dependence becomes weaker when the strain rate increases. As can be seen from Figure 2, the effect of the compression conditions on the peak stress is smaller at high strain rates than at the other strain rates. In other words, we find that the DRX behavior of the present alloy is influenced by the strain rate in addition to the well-known dependence of the grain size on the Z parameter. Because these phenomena are observed at high strain rates, it is essential to consider the effect of the temperature rise due to adiabatic heating. The temperature increment can be estimated from the shape of the σ-ε curve using the method described in Reference 16. The higher the Z parameter, the higher the temperature rise; it reaches a maximum of approximately 60 K (60 pct compression) under the deformation conditions in the present study. The results for 1050 °C and 10 s^{-1} are indicated by an arrow in Figure 13, which

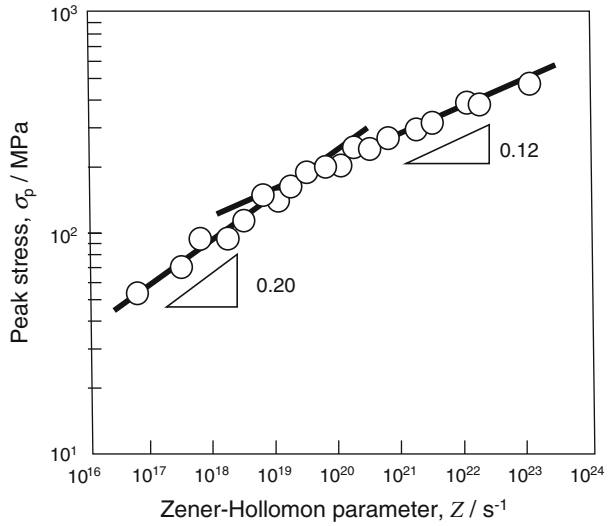

Fig. 14—Relationship between peak flow stress and Z parameter in hot-compression test.

shows that there is a difference of two orders of magnitude from the value of the Z parameter estimated using Eq. [3]. Therefore, a temperature rise of more than 250 °C is required to assure conformity with Eq. [3]; thus, work heating has a limited effect. On the other hand, the Z-parameter dependence of the peak stress σ_p varies for both a low and a high Z parameter, as can be seen from Figure 14. The slope m of the Z parameter dependence of the peak stress σ_p (indicated by the straight line in Figure 14) begins to change at approximately $10^{19} < Z < 10^{20}$. This suggests that the deformation mechanism changes before and after this value of the Z parameter. In addition, the d-Z relation shown in Figure 13 starts to show scatter from the vicinity of $Z \sim 10^{19}$, suggesting that such a d-Z relation is caused by a deformation mechanism that is different from that for high strain rates of over 10 s^{-1}. This is supported by the fact that the strain-rate dependence of the 0.2 pct yield stress at various deformation temperatures becomes negative for strain rates higher than 1.0 s^{-1} (Figure 3). However, further study is necessary to ascertain the kind of deformation mechanism that is operative.

B. *Estimation of SFE Based on Thermodynamic Calculations*

As mentioned earlier, the SFE greatly affects high-temperature deformation and DRX behavior. Therefore, the SFE of the Co-29Cr-6Mo alloy at the hot-compression test temperature was estimated by performing thermodynamic calculations.

Olson and Cohen have proposed a method for thermodynamically calculating the SFE of alloy systems that undergo a phase transformation from an fcc structure into an hcp structure.[13] It is given by the sum of a volumetric energy term and a surface energy term, as given by

$$\gamma = 2\rho\Delta G^{\gamma\to\varepsilon} + 2\sigma^{\gamma/\varepsilon} \quad [4]$$

Table III. Material Constants Used in Calculation of Stacking-Fault Widths

Symbol	Nomenclature	Value
$2\sigma^{\gamma/\varepsilon}$	surface energy of the interface γ/ε (mJ m^{-2})	15
a	lattice constant (nm)	0.354
N	Avogadro's number (mol^{-1})	6.022×10^{23}
G	shear modulus (GPa)	88
b_p	magnitude of Burgers vectors of the partial dislocations (nm)	0.145
v	Poisson's ratio	0.28
m	Schmid factor	0.326
γ	SFE (mJ m^{-2})	
	1050 °C	29.1
	1100 °C	36.2
	1150 °C	43.3
	1200 °C	50.4

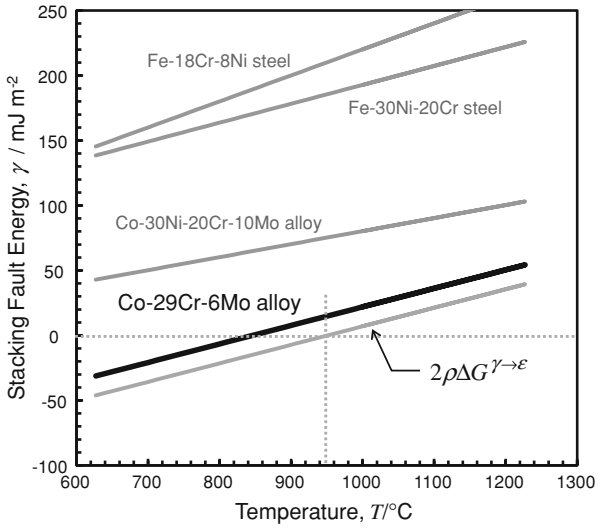

Fig. 15—Temperature dependence of SFEs using a thermodynamic model.

where $\Delta G^{\gamma\to\varepsilon}$ and $\sigma^{\gamma/\varepsilon}$ are the Gibbs energy difference and the interface energy between the γ and ε phases, respectively. The value of ρ is the atomic density of the $\{111\}_\gamma$ plane per mole, which is given by

$$\rho = \frac{4}{\sqrt{3}}\frac{1}{a^2 N} \quad [5]$$

The values used in the calculation are given in Table III. Figure 15 shows the calculation results for the SFE in the neighborhood of the deformation temperature of the hot-compression test. For comparison, the values of SFE are also presented for the Co-39Ni-20Cr-10Mo alloy (SPRON510), in which the γ phase is stabilized by Ni addition, the SUS304 austenitic stainless steel (Fe-18Cr-8Ni) (an example of a low-SFE alloy), and the 800H high-nickel steel (Fe-30Ni-20Cr). Because the temperature dependence of the interfacial energy in Eq. [4] is negligible and its value does not change even for transition metals,[19] the interfacial energy term is

assumed to be $2\sigma^{\gamma/\varepsilon} = 15$ mJ m^{-2} in this calculation.[31] The SFE of the Co-29Cr-6Mo alloy, 30 to 50 mJ m^{-2} at the hot-compression test temperature (Figure 15), is extremely low. This is because the SFE and its temperature dependence reflect the stabilities of the γ and ε phases. The temperature (T_0) at which the Gibbs free energies of the γ and ε phases of the Co-29Cr-6Mo alloy are equal is approximately 950 °C, which is very close to the hot-deformation temperature. Furthermore, the calculated SFE becomes negative at temperatures lower than 850 °C. This is because the ε phase becomes stable in that temperature range, making $\Delta G^{\gamma\to\varepsilon}$ negative. The stabilities of the γ phase and the austenitic phase of the fcc structure of the SPRON510, SUS304, and 800H at room temperature are relatively high compared to those of the Co-29Cr-6Mo alloy; consequently, they have larger SFEs. When the results for the SUS304 are extrapolated to room temperature, an SFE of approximately 30 mJ m^{-2} is obtained, which is close to a previously reported value.[17] The temperature dependences of the SFEs for Co and Co-Ni alloys have been reported by Ericsson.[32] Although the SFE is thermodynamically calculated by considering only the Gibbs energies of the γ and ε phases, it increases linearly with temperature, and the value obtained by adding the interfacial energy term to it agrees with the results for the Co-29Cr-6Mo and SPRON510 alloys. Therefore, the SFEs and their temperature dependences obtained using Thermo-Calc software are considered to be reliable.

C. *Dislocation Structure Formed by Hot Deformation*

In an fcc alloy with a low SFE, perfect dislocations with Burgers vectors $a/2[\bar{1}01]$ tend to dissociate into Shockley partial dislocations bounding the stacking fault in the {111} plane, in accordance with the following equation:

$$\frac{a}{2}[\bar{1}01] \rightarrow \frac{a}{6}[\bar{2}11] + \text{stacking fault} + \frac{a}{6}[\bar{1}\bar{1}2] \qquad [6]$$

The width w of the Shockley partials connected by a stacking fault is defined as the distance at which the attractive force to minimize the SFE equals the repulsive force of the partial dislocation. A model that considers the effect of applied stress on a dislocation dissociation has recently been proposed by Byun[33] and is given by

$$w = \frac{Gb_p^2}{\pi(2\gamma - \tau b_p|\sin\theta_2 - \sin\theta_1|)} \times \left(\cos\theta_1\cos\theta_2 + \frac{\sin\theta_1\sin\theta_2}{1-\nu}\right) \qquad [7]$$

where G is the shear modulus, b_p is the magnitude of the Burgers vector of a partial dislocation, τ is the shear stress, θ_1 and θ_2 are the angles of the Burgers vectors of the leading and trailing partials, respectively, with the dislocation line vector of the perfect dislocation, and ν is the Poisson's ratio. Figure 16 shows an example of a calculation of the stacking-fault width under a uniaxial deformation that corresponds to the tension/compression

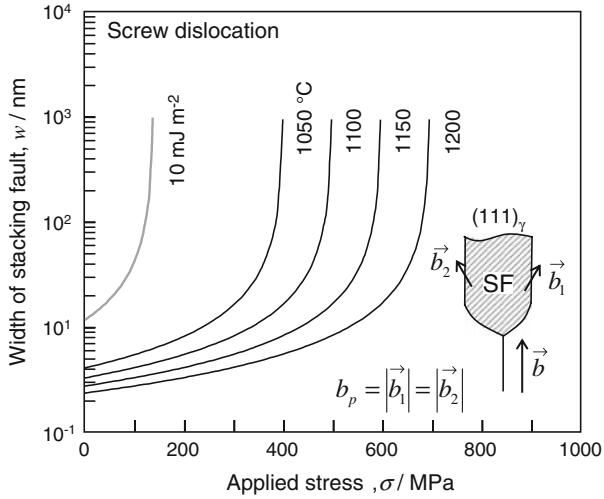

Fig. 16—Stress dependence of width of stacking fault on applied stress at various temperatures.

test. In this calculation, the perfect dislocation prior to the partial dislocation in the Co-29Cr-6Mo alloy was assumed to be a screw dislocation, and $m = 0.326$ was used as the mean Schmid factor of the fcc alloy for plotting the uniaxial tensile/compression stress along the horizontal axis. This is shown together with an example when $\gamma = 10$ mJ m^{-2}. Figure 16 shows that the stacking-fault width gradually increases with an increase in the applied stress, until it reaches a critical stress, at which point the stacking fault increases sharply and then diverges. The critical stress for the divergence of the stacking fault decreases with the SFE. Moreover, because the SFE should always be positive, based on the discussion in Section B, the SFE of the present alloy can be considered to be almost zero for a wide range of temperatures, from room temperature to a high temperature. In addition, the dislocation induced by the deformation process dissociates as the temperature is increased from room temperature to a high temperature (in some cases, the dissociation width is divergent), resulting in a dislocation structure with a high planarity. In fact, as illustrated in Figure 17, the unrecrystallized deformation microstructure induced in the Co-29Cr-6Mo alloy after the hot compression by 20 pct at 1150 °C at a strain rate of 10 s^{-1} exhibits a large number of stacking faults, linear contrasts, and localized slip, and it appears similar to those induced in the cold working of austenitic stainless steels that has an SFE of 10 to 30 mJ m^{-2} at room temperature.[19] These results indicate that the structure of the dislocation induced by deformation is governed primarily by the value of the SFE, even if the deformation temperatures are different. The results also indicate that high-temperature deformation of the Co-29Cr-6Mo alloy tends to be induced inhomogeneously, similar to the case of cold working. Finally, the results show that the formation of inhomogeneous dislocation distributions and the accumulation of geometrically necessary (GN) dislocations, which play an important role in the nucleation of recrystallized grains during hot deformation, are effectively promoted.

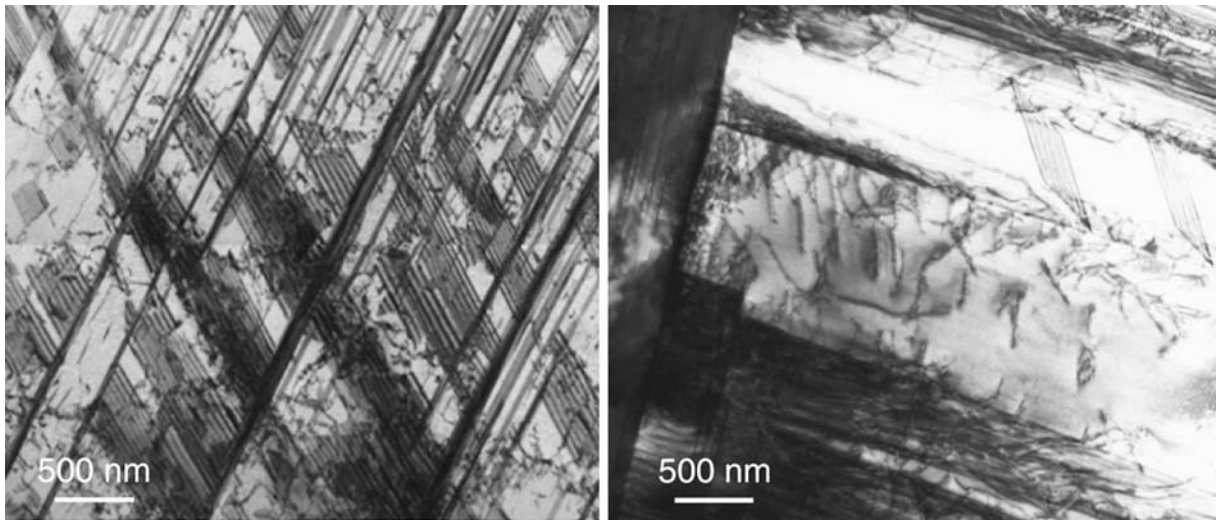

Fig. 17—TEM micrographs showing dislocation structure induced after deformation by 20 pct at 1150 °C at a strain rate of 1.0 s^{-1}.

D. *Nucleation of Dynamically Recrystallized Grains*

Dynamic recrystallization at high temperatures is generally considered to be a discontinuous process controlled by the nucleation and subsequent growth of new grains and driven by the strain energy accumulated by deformation. Because serration of the GBs cannot be clearly confirmed in the DRX of the Co-29Cr-6Mo alloy, nucleation is assumed to occur by some mechanism other than bulging. We therefore discuss the DRX behavior of the present alloy from the viewpoint of nucleation and its driving force.

1. *Nucleation sites of new grains*

Figures 18(a) through (d) show the EBSD results for a specimen compressed by 60 pct at 1050 °C at a strain rate of 10^{-2} s^{-1}. The nonrecrystallized regions are assumed to represent the microstructural features related to those of the dynamically recrystallized new grains. Lattice distortions introduced during hot deformation are observed in the nonrecrystallized region as local misorientations (orientation gradations) in the IPF map of Figure 18(a). These are also obvious in the kernel average misorientation (KAM) map (Figure 18(b)), which shows a difference in the crystal orientations of adjacent measurement points measured by the EBSD method and which clearly shows that there is a large local orientation difference between the coarse, nonrecrystallized region and the surrounding fine grains. This local orientation difference results from the GN dislocations. Large local orientation differences occur not only in the vicinity of GBs, where there are large three-dimensional constraints, but also within grains. Some of these regions with high KAMs overlap with low-angle grain boundaries (LAGBs) that have misorientations of $2 \text{ deg} < \theta < 15 \text{ deg}$ (indicated by white lines in the figure). Figure 18(d) shows the misorientation profile along the arrow in Figure 18(a) with a step interval of 0.2 μm. A maximum point-to-point dispersion of approximately 3 deg is observed, and large misorientations, corresponding to LAGBs, are sporadically observed. These LAGBs are thought to form as a result of an increase in the GN dislocation density. On the other hand, a cumulative (point-to-origin) profile indicates large misorientations of more than 20 deg, even within a single grain over a measurement distance of 30 μm. The resultant large local misorientation leads to the strain-induced grain subdivision during straining. Similar results have been found in an aluminum alloy subjected to ECAP in a warm temperature range and they were ascribed to deformation-induced sub-boundaries.[4] Even for an aluminum alloy, such a microstructure requires a true strain of 2 to 4 and this phenomenon is ascribed to grain refinement caused by the continuous DRX associated with grain subdivision. On the other hand, it is difficult to conceive that such subdivision of the initial grains can occur in conventional compression tests, which have true strains of less than 1, especially when the initial microstructure consists of a single phase. Consequently, it is concluded that the grain refinement in the Co-29Cr-6Mo alloy progresses in such a manner that a localized form of "continuous" DRX occurs due to the effective introduction of local misorientation during the deformation process, caused by the high planarity of the dislocation structure mentioned earlier (*e.g.*, Figure 17).

Figure 19 shows the TEM image from the vicinity of the interface between the nonrecrystallized region and the continuous dynamic recrystallized grains in the sample compressed by 60 pct at 1050 °C at 0.1 s^{-1}. The lamellar-like contrasts are visible in the nonrecrystallized region in the bright-field image of Figure 19(a). On the other hand, streaks caused by stacking faults are confirmed in the direction of $[111]_\gamma$ in the SAD pattern (Figure 19(b)), from the region indicated by the white circle. Therefore, it is assumed that the contrasts originate from a large number of stacking faults formed by the dissociation of perfect dislocations in the $\{111\}_\gamma$ plane, as seen in the bright-field image. Also, the key diagram of the SAD pattern in Figure 19(b)

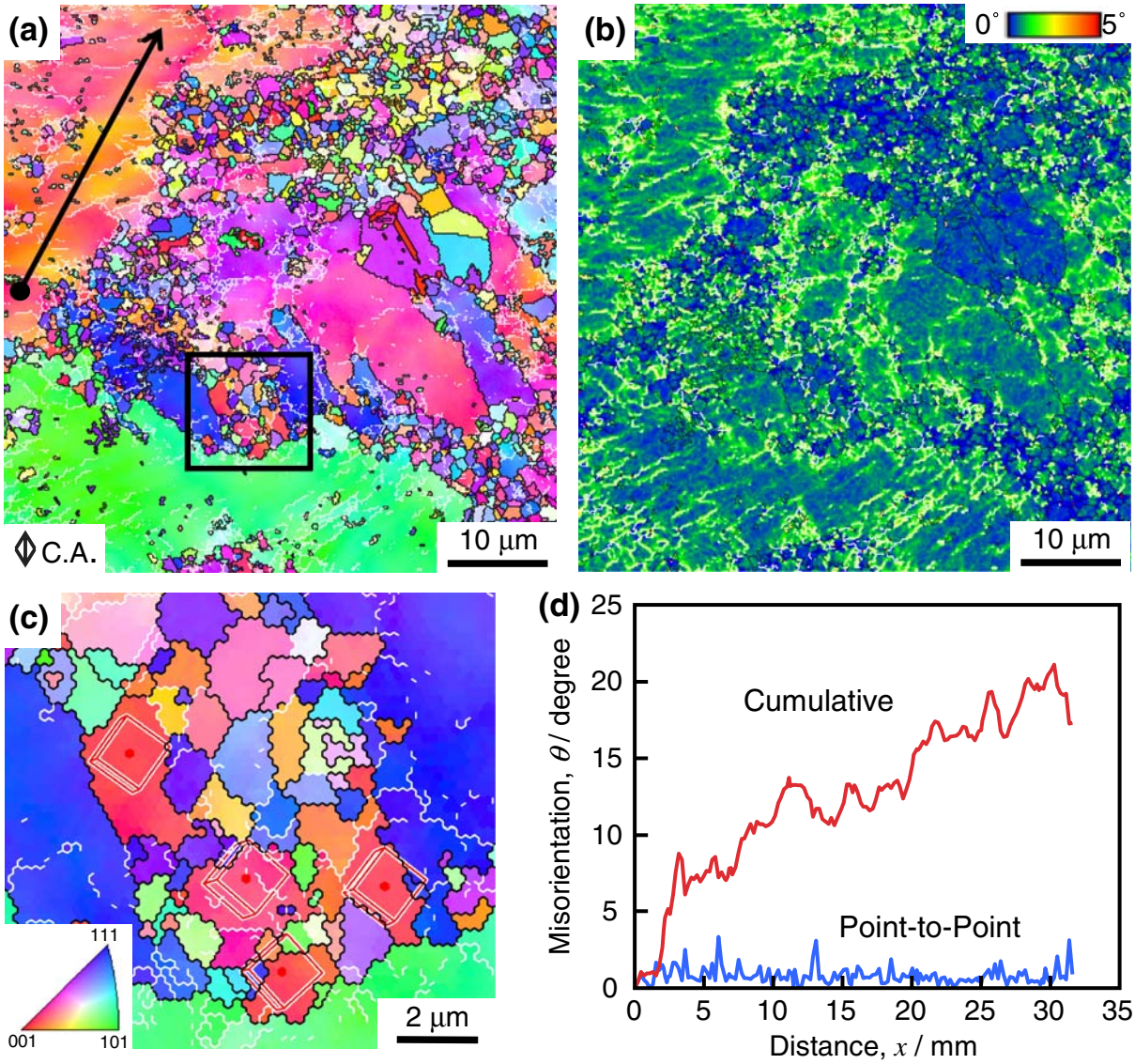

Fig. 18—Orientation imaging maps and misorientation analysis of specimen deformed at 1050 °C at 10^{-2} s^{-1} obtained using FESEM/EBSD method: (*a*) IPF map, (*b*) KAM map, and (*c*) magnified IPF map of area outlined in rectangular in (a). (*d*) Misorientation profile along the arrow in (a). Black and white lines indicate the HAGBs and LAGBs, respectively.

(Figure 19(c)) shows the Shoji–Nishiyama orientation relationship attributed to the martensitic transformation. From the earlier discussion, it is assumed that the nonrecrystallized region consists of the γ phase with a planar dislocation structure caused by the dissociated dislocations and the martensitic ε phase on the order of nanometers. Although it is difficult to determine whether the ε phase is generated by athermal or strain-induced martensitic transformation, we can conclude that the present alloy has an extremely low SFE even at high temperatures. Consequently, it is assumed that the grain subdivision shown in Figure 18 is caused by an inhomogeneous deformation promoted by planar dislocation slip, as shown in Figure 17.

Tsuji *et al.* conducted a quantitative study on the SRX and DRX in ferritic iron and found that the nucleation in recrystallization cannot be explained only by the magnitude of the driving force but that it depends largely on the local misorientation, *i.e.*, the inhomogeneous deformation.[34,35] They also concluded that DRX occurs in response to the deformation conditions (temperature, strain rate, and strain), provided sufficiently large orientation differences are formed during deformation. Therefore, the local misorientation distributions observed in the EBSD measurements described earlier satisfy the requirement for DRX nucleation. Figure 18(c) shows a magnified image of the region enclosed by a square on the IPF map shown in Figure 18(a). It shows that fine grains are formed from initial grains that have crystal orientations close to $[111]_{\gamma}$. Grains that have approximately the same crystal orientations marked by the unit cell model are considered to originate from grains that were fragmented through the refinement process occurring during DRX. This suggests that the subdivision of initial grains occurs through the formation of regions surrounded by the GN

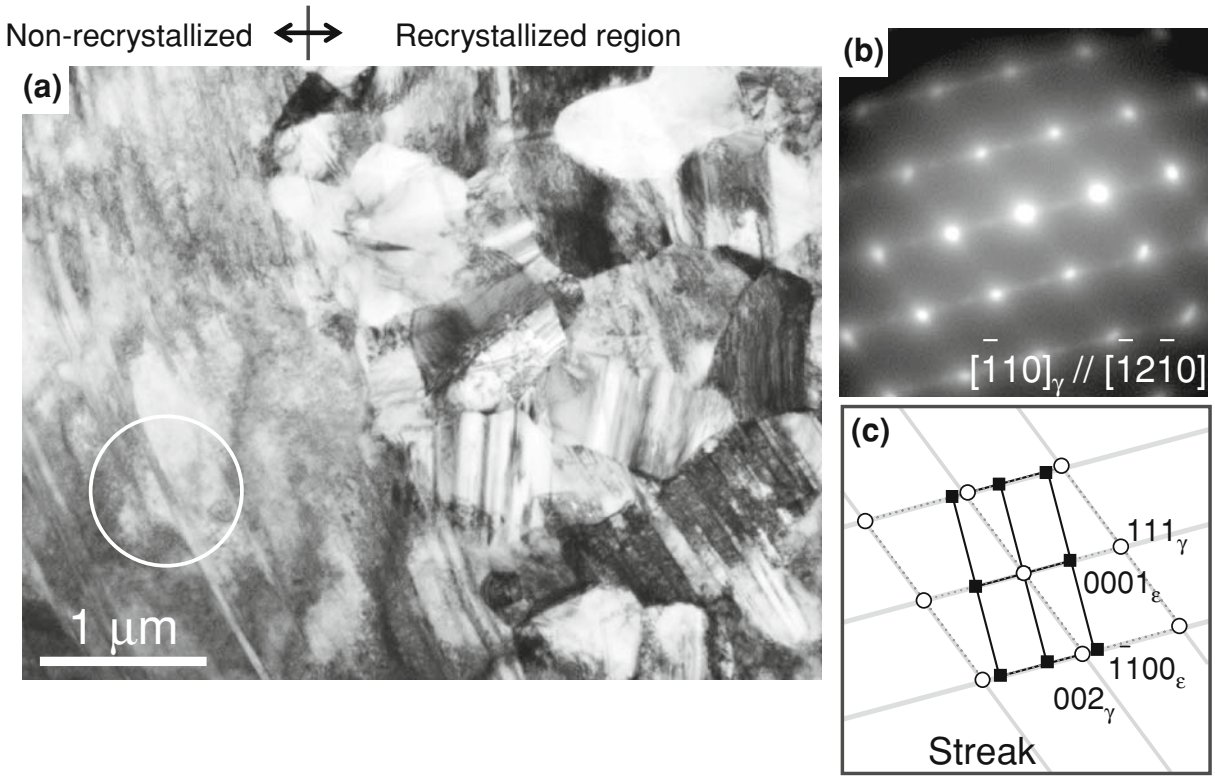

Fig. 19—TEM microstructure of interface between nonrecrystallized and recrystallized region of specimen after 60 pct compression at 1050 °C at 1.0 s^{-1}: (*a*) bright-field image micrograph, (*b*) SAD pattern of nonrecrystallized region, and (*c*) key diagram of the SAD pattern.

boundaries, which contain a high density of GN dislocations (*e.g.*, dense dislocation walls (DDWs)) originating from inhomogeneous deformation. Areas with relatively high misorientations are anticipated to transform themselves into a new grain enclosed by HAGBs. Because regions of high-GN dislocation density are energetically unstable, the formation of HAGBs is thought to occur rapidly, simply by atomic diffusion during high-temperature deformation. Further investigation, however, is required to confirm this.

2. *Driving force of nucleation of DRX grains*

The driving force of DRX when inhomogeneous strains are introduced is explained as follows.[34] The local misorientation (lattice curvature), namely, the lattice distortion, is formed as GN dislocations are induced in the vicinity of the interface between regions that have different crystal orientations; the density of the GN dislocations ρ_{dis} is expressed by

$$\rho_{dis} = \frac{2\theta}{bD} \quad [8]$$

where θ is the local misorientation, b is the magnitude of the Burgers vector, and D is the mean intercept length (for example, the spacing between sub-boundaries). If we assume that the nucleation of DRX commences in a region in which there is a large local misorientation, the dislocation density that becomes the driving force will be strongly affected by GN dislocations induced to compensate the crystal orientation difference. Therefore, the stored energy ΔE due to the accumulation of GN dislocations can be expressed as follows:

$$\Delta E = \rho_{dis}\frac{Gb^2}{2} = \frac{Gb\theta}{D} \quad [9]$$

where G is the shear modulus. Equation [9] implies that the stored energy increases as the local misorientations increase and the mean intercept length decreases. Wang *et al.*[36] discussed the nucleation of the DRX of Fe-30Ni-20Cr alloy in terms of the local stored energy that results from the misorientation caused by the high density of DDWs. Because large lattice distortions are observed in the nonrecrystallized microstructures in the hot deformation of the present alloy, there must be a large nucleation driving force. Hence, the DRX behavior is qualitatively explained as a combined result of the high nucleation probability caused by lattice distortions and the enhanced driving force due to the local stored energy of the lattice curvatures; this is supported by the experimental results for the present alloy. These features that relate to DRX are strongly associated with the extremely low SFE of the present alloy, even at high temperatures.

V. CONCLUSIONS

Hot-compression tests were conducted on the Co-29Cr-6Mo alloy, which is used for biomedical applications, for various deformation temperatures and strain rates. The true stress-true strain curves

obtained from the hot-compression tests under all compression conditions exhibited DRX characteristics. The DRX was confirmed by both FESEM/EBSD and TEM observations. The grain size after hot deformation can be classified based on the Z parameter; it became finer with an increase in the Z parameter. On the other hand, as the strain rate increased from 0.1 to 10 s^{-1}, the dependence of the dynamically recrystallized grain size on the Z parameter changes and the grains become coarser.

The SFEs of the present alloy at the hot-compression test temperature were estimated to be 30 to ~50 mJ m^{-2} using a thermodynamic model and were extremely low compared to those of other alloys. The apparent SFE is considered to decrease due to the external stress, which causes the planarity of the dislocation structure, promoting inhomogeneous deformation. This suggests that the deformation structure is determined explicitly by the SFE, even at high temperatures. A large local misorientation is confirmed in the nonrecrystallized region by the FESEM/EBSD observations. Nucleation of the DRX grains of the present alloy can be explained based on the lattice distortion model, which has been reported. It is also estimated that the large local misorientation associated with GN dislocations is responsible for the nucleation driving force. The fact that the local misorientation is caused by inhomogeneous dislocation distributions rather than the applied strain explains why the DRX behavior of the Co-29Cr-6Mo alloy is greatly affected by the SFE, which is extremely low, even at high temperatures.

ACKNOWLEDGMENT

This research was supported by the Cooperation of Innovative Technology and Advanced Research in Evolutional Area under the Ministry of Education, Culture, Sports, Science and Technology (Tokyo, Japan).

REFERENCES

1. A. Chiba, K. Kumagai, H. Takeda, and N. Nomura: *Mater. Sci. Forum*, 2005, vols. 475–479, pp. 2317–22.
2. R. Valiev: *Nat. Mater.*, 2004, vol. 3, pp. 511–16.
3. Y. Fukuda, K. Oh-ishi, Z. Horita, and T.G. Langdon: *Acta Mater.*, 2002, vol. 50, pp. 1359–68.
4. O. Sitdikov, T. Sakai, E. Avtokratova, R. Kaibyshev, K. Tsuzaki, and Y. Watanabe: *Acta Mater.*, 2008, vol. 56, pp. 821–34.
5. Y. Saito, N. Tsuji, H. Utsunomiya, T. Sakai, and R.G. Hong: *Scripta Mater.*, 1998, vol. 39, pp. 1221–27.
6. Y. Saito, H. Utsunomiya, N. Tsuji, and T. Sakai: *Acta Mater.*, 1999, vol. 47, pp. 579–83.
7. A. Belyakov, T. Sakai, H. Miura, R. Kaibyshev, and K. Tsuzaki: *Acta Mater.*, 2002, vol. 50, pp. 1547–57.
8. J. Xing, X. Yang, H. Miura, and T. Sakai: *Mater. Trans.*, 2008, vol. 49, pp. 69–75.
9. T. Sakai and J.J. Jonas: *Acta Metall.*, 1984, vol. 32, pp. 189–209.
10. A. Belyakov, H. Miura, and T. Sakai: *Mater. Sci. Eng., A*, 1998, vol. A255, pp. 139–47.
11. A.M. Wusatowska-Sarnek, H. Miura, and T. Sakai: *Mater. Sci. Eng., A*, 2002, vol. A323, pp. 177–86.
12. C. Sommitsch and W. Mitter: *Acta Mater.*, 2006, vol. 54, pp. 357–75.
13. N. Tsuji, Y. Matsubara, and Y. Saito: *Scripta Mater.*, 1997, vol. 37, pp. 477–84.
14. H. Yagi, N. Tsuji, and Y. Saito: *Tetsu-to-Hagané*, 2000, vol. 86, pp. 349–56.
15. H. Monajati, M. Jahazi, S. Yue, and A.K. Taheri: *Metall. Mater. Trans. A*, 2005, vol. 36A, pp. 895–905.
16. Y.P. Li, E. Onodera, H. Matsumoto, and A. Chiba: *Metall. Mater. Trans. A*, 2009, vol. 40A, pp. 982–90.
17. J. Talonen and H. Hänninen: *Acta Mater.*, 2007, vol. 55, pp. 6108–18.
18. G.B. Olson and M. Cohen: *Metall. Trans. A*, 1976, vol. 7A, pp. 1897–1904.
19. S. Allain, J.-P. Chateau, O. Bouaziz, S. Migot, and N. Guelton: *Mater. Sci. Eng., A*, 2004, vols. A387–A389, pp. 158–62.
20. Y.V.R.K. Prasad: *JMEPEG*, 2003, vol. 12, pp. 638–45.
21. S.H. Lee, T. Uchikanezaki, N. Nomura, M. Nakamura, and A. Chiba: *Mater. Trans., JIM*, 2007, vol. 48, pp. 1084–88.
22. A. Chiba, S.H. Lee, H. Matsumoto, and M. Nakamura: *Mater. Sci. Eng.*, 2009, vols. 513–514, pp. 286–93.
23. Ika Kartika, H. Matsumoto, and A. Chiba: *Metall. Mater. Trans. A*, 2009, vol. 40A, pp. 1457–68.
24. P. Huang and H.F. López: *Mater. Lett.*, 1999, vol. 39, pp. 249–53.
25. T. Maki and I. Tamura: *Tetsu-to-Hagané*, 1984, vol. 15, pp. 2073–80.
26. C.M. Sellars and W.J.McG. Tegart: *Mem. Sci. Rev. Met.*, 1966, vol. 63, pp. 731–45.
27. Nippon Kinzoku Gakkai: *Kinzoku Data Book*, 4th ed., Maruzen, Tokyo, 2004, p. 21.
28. L.X. Li, Y. Lou, L.B. Yang, D.S. Peng, and K.P. Rao: *Mater. Des.*, 2002, vol. 23, pp. 451–57.
29. X. Fang, D. Yi, B. Wang, C. Wu, and H. Zhang: *Rare Met.*, 2008, vol. 27, pp. 121–26.
30. I. Salbatori, T. Inoue, and K. Nagai: *ISIJ Int.*, 2002, vol. 42, pp. 744–50.
31. A.P. Miodownik: *CALPHAD*, 1978, vol. 2, pp. 207–26.
32. T. Ericsson: *Acta Metall.*, 1966, vol. 14, pp. 853–65.
33. T.S. Byun: *Acta Mater.*, 2003, vol. 51, pp. 3063–71.
34. N. Tsuji, T. Shinmiya, Y. Saito, and M. Muraki: *ISIJ Int.*, 1998, vol. 38, pp. 380–89.
35. N. Tsuji, Y. Matsubara, Y. Saito, and T. Maki: *J. Jpn. Inst. Met.*, 1998, vol. 62, pp. 967–76.
36. X. Wang, E. Brünger, and G. Gottstein: *Mater. Sci. Eng., A*, 2000, vol. A290, pp. 180–85.